Available online at www.sciencedirect.com

ScienceDirect

Procedia CIRP 126 (2024) 555–560

www.elsevier.com/locate/procedia

17th CIRP Conference on Intelligent Computation in Manufacturing Engineering (CIRP ICME '23)

Low-temperature tensile properties of meta-stable β titanium Ti-5Al-5V-5Mo-3Cr alloy fabricated by pulsed laser powder bed fusion

Akshay Ashok Benni*, Francesco Galbusera, Ali Gökhan Demir, Barbara Previtali

Department of Mechanical Engineering, Politecnico di Milano, 20156 Milan, Italy

* Corresponding author. *E-mail address:* akshayashok.benni@polimi.it

Abstract

Ti-5Al-5V-5Mo-3Cr (Ti-5553) alloy is increasingly used in structural airplane components, such as landing gear and fuselage, thanks to its high strength, good ductility, and low density. These components are consistently subjected to sub-zero temperatures during the flight. In this study, pulsed laser powder bed fusion (L-PBF) parameters were firstly optimized to fabricate highly dense (>99%) parts, and their effect on microstructure and microhardness was analyzed. Finally, tensile properties were evaluated under sub-zero temperature conditions and compared to the standard room ones to validate the feasibility of using Ti5553 under low-temperature environments.

Keywords: Laser powder bed fusion; Metastable titanium; Ti-5Al-5V-5Mo-3Cr; Sub-zero tensile properties

1. Introduction

Titanium alloys, particularly the Ti-6Al-4V (Ti-64), have been popular in aerospace applications for some time, making the majority of the Ti alloys used. However, metastable β alloys have seen renewed interest in recent years [1]–[3]. Among them, the newer commercial metastable β-Ti alloy Ti-5Al-5V-5Mo-3Cr (Ti-5553) was introduced by Titanium Metals Cooperation and popularized due to improvements in its processability, cost reduction and higher strength and heat treatability over the previous metastable β-Ti alloys. Ti-5553 is widely used in structural elements such as landing gears, fuselage, and airframes owing to its higher strength, toughness, and corrosion resistance [4]–[7]. These properties, coupled with the advantages of Additive manufacturing (AM) and the problems related to the machining of metastable β-Ti alloys, make them great potential for AM fabrication [7].

Nomenclature

d_h	Hatch distance (µm)
d_p	Point distance (µm)
E	Energy density (J/mm³)
El	Elongation at fracture (%)
HT	Heat treated
P	Laser power (W)
RT	Room temperature (°C)
SZT	Sub-zero temperature (°C)
ST	Solution treated
t_{on}	Exposure time (µs)
UTS	Ultimate tensile strength (MPa)
YS	Yield strength (MPa)
z	Layer thickness (µm)

2212-8271
10.1016/j.procir.2024.08.239

Processability of highly dense specimens of the Ti-5553 has been established with conventional L-PBF systems operating in continuous or pulsed emission mode of laser [8]–[12]. Regimes of spatial and temporal profiles of both the emission modes and their effect on the depositions are discussed in the literature [13].

With regards to Ti-5553, similar to the Ti-64 alloy, lack of fusion pores are seen at low energy density, due to insufficient availability of energy to fuse the subsequent layers completely. On the other hand, keyhole defects are observed at high energy densities with the optimal process window existing between the two ends [8], [10].

Pure β grain structure is generally seen without a second phase or grain boundary alphas; however, Ramachandiran et al.[8], and Bakhshivash et al. [10] separately observed α precipitation within the β matrix at high energy densities. While Schwab et al. made a similar observation using a pre-heated substrate at 500 °C [12]. The above findings indicate an effect of cooling rates on the presence and extent of precipitation seen in L-PBF Ti-5553.

Generally, lack of alphas precipitates results in isotropic tensile properties in β alloys. However, Zafari et al. [9] reported slightly better tensile properties in perpendicular orientation to the build direction compared to the parallel orientation. Work softening is observed for an orientation parallel to the build direction, while work hardening was seen in an orientation perpendicular to the build direction. Post-processing and heat treatments are seen to reduce anisotropy.

Limited research is available on the L-PBF of the alloy with a pulsed laser mode investigating the effects of individual process parameters. Furthermore, to the best of the author's knowledge, a lack of research on the sub-zero tensile properties of the L-PBF Ti-5553 is seen in the open literature available. Considering the structural applications at low temperatures and temperature sensitivity of β-Ti alloys [14], [15], the present research aims to investigate the effect of sub-zero temperature environment on the tensile behaviors of the Ti-5553 L-PBF alloy. Firstly, a preliminary analysis was carried out to identify the optimal process parameters, and high relative density was achieved in the printed parts. Then, grain morphology and microstructure were studied. Finally, tensile samples were fabricated to investigate the tensile properties at room and sub-zero temperatures of -50 °C.

2. Materials and Methodology

2.1. Material

In the present research, Ti-5553 powder with particle size ranging between d_0=15 and d_{90}=53 µm supplied by AP&C (a GE additive company) with the nominal composition shown in *Table 1* was used along with Ti-6Al-4V substrate.

Table 1. Nominal chemical composition of Ti-5553 powder used in wt%

Element	Al	Ti	V	Mo	Cr	Fe
wt (%)	5.1	Bal.	4.9	5.0	2.9	0.41

2.2. Experimental design

To determine the optimal process parameters, sets of 5x5x10 mm^3 cubes were realized. A commercial L-PBF Renishaw AM250 machine equipped with the reduced build volume unit (RBV) was employed in pulsed laser mode under argon processing gas. Parameter optimization was performed at fixed laser power (P) of 200 W, layer thickness (z) of 30 µm, and spot size of 70 µm. In comparison, other parameters were varied at three levels, with hatch distance (d_h) between 50 and 80 µm, exposure time (t_{on}) between 40 and 80 µs, and point distance (d_p) between 60 and 90 µm. Two replicates of each variable parameter condition were considered. A meander scanning strategy with a hatch rotation angle of 67° between successive layers was used. The list of fixed and varied parameters is given in Table 2.

Relative densities were measured using Image J (U.S. National Institutes of Health, Bethesda, Maryland, USA) software on the metallographic cross-sections acquired from an optical microscope (Leitz Ergolux 200). Chemical etching was done with Kroll's reagent (HNO_3 (5-7%), HF (2-4%), H_2O (bal.)). Vickers microhardness measurements were carried out according to ASTM E384 with a load of 300 gf and a dwell time of 10 s, using a mechanical indenter (MH3, Metkon®, Bursa, Turkey). Tensile tests were carried out according to ISO-6892 at room and sub-zero temperatures (-50 °C) with a universal testing machine (Alliance RT/100, MTS Landmark®, Turin, Italy). Cylindrical dog bone-shaped tensile samples of a total length of 49 mm and M8 threaded gripping ends with a gauge length of 20 mm and an original diameter (gauge diameter) of 4 mm were machined from the printed rectangular blocks. An environmental chamber was used with liquid nitrogen to obtain sub-zero testing conditions. Fracture surface micrographs were acquired using a Scanning Electron microscope (ZEISS Sigma, Oxford Instruments plc, Oxfordshire, UK).

Table 2. List of fixed and varied parameters in the experimental campaign

Fixed parameters	Value
Laser power, P(W)	200
Spot diameter (µm)	70
Layer thickness, z(µm)	30
Hatch scan strategy	Meander
Hatch angle, (°)	67
Varied parameters	**Value**
Hatch distance, d_h (µm)	50,65,80
Exposure time, t_{on} (µs)	40,60,80
Point distance, d_p (µm)	60,75,90

3. Results and discussion

3.1. Identification of optimal process parameters

The main effect plot of the relative density (ρ) is shown in Fig. 1a. It is seen that exposure time and point distance have the most significant influence on the relative density, while the hatch distance effect is less significant compared to these two parameters. In Fig. 1b, the interaction plot is seen, which shows

the effect of the interaction of parameters on the relative density. Intersecting lines indicate an influence of the interaction, as seen, interaction between t_{on} and d_p indicates strong influence and a possible influence of interaction between t_{on} and d_h. This can be confirmed by the analysis of variance (ANOVA) seen in Table 3, the interaction of t_{on} and d_p has the most significant effect on the relative density, followed by the low effect of the interaction of d_h and t_{on}.

$$E = \frac{P * t_{on}}{d_p * d_h * z} \quad (1)$$

Table 3. Analysis of variance on density and model summary

Source	DF	Adj SS	Adj MS	F-Value	P-Value
d_h (µm)	1	0.0485	0.04853	0.57	0.471
t_{on} (µs)	1	6.0037	6.00367	70.06	**0**
d_p (µm)	1	6.645	6.64497	77.55	**0**
d_h (µm)*t_{on} (µs)	1	0.7489	0.74893	8.74	**0.016**
d_h (µm)*d_p (µm)	1	0.4257	0.42573	4.97	0.053
t_{on} (µs)*d_p (µm)	1	8.2477	8.24767	96.25	**0**
Error	9	0.7712	0.08569		
Total	16	25.2459			

Model Summary			
S	R^2	R^2_{adj}	R^2_{pred}
0.292731	96.95%	94.57%	85.35%

The experimental campaign was carried out in the energy density (calculated with equation 1) range of 37 to 178 J/mm³. As Fig. 2 shows, high levels of irregular pores were present at low energy density, with circular pores seen at higher energy density. Low porosity was obtained in the mid-range of energy density, consistent with the literature. In the present work, ρ > 99.5 % are obtained in the energy density range of 75-125 J/mm³. Accordingly, the specimen produced with d_h = 80 µm, t_{on} = 80 µm, and d_p = 60 µm that guaranteed the highest density was chosen for further metallographic characterization and mechanical properties (microhardness and tensile tests).

3.2. Microstructure

Etched cross-sections in the longitudinal direction are shown in Fig. 3 for the cube with the highest density. Fig. 3 (a-c) shows microstructure in the cube's top, middle, and bottom region, with irregular columnar prior-β grain structures along the build direction visible through the entire cross-section. No significant difference was observed between the three regions. Fig. 3d shows the prior-β grain boundary, while the higher magnification image in Fig. 3e shows the melt pool boundaries and the cellular dendritic structures near the melt pool boundary. These cell structures are attributed to the constitutional supercooling during solidification brought about by repeated remelting of the deposited layers [9], [16], [17].

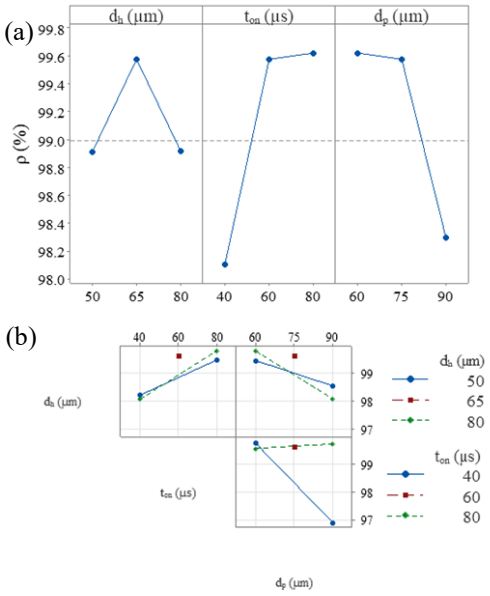

Fig. 1. (a) Main effects plot of relative density, and (b) interaction plot of relative density

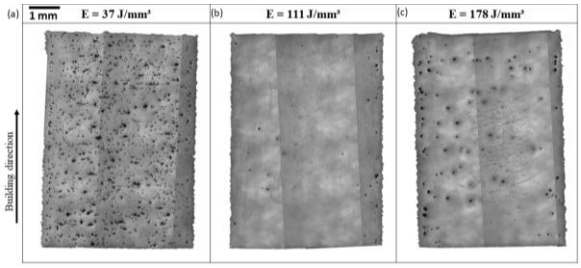

Fig. 2. Metallographic cross-section at (a) low energy density, (b) medium energy density, and (c) high energy density

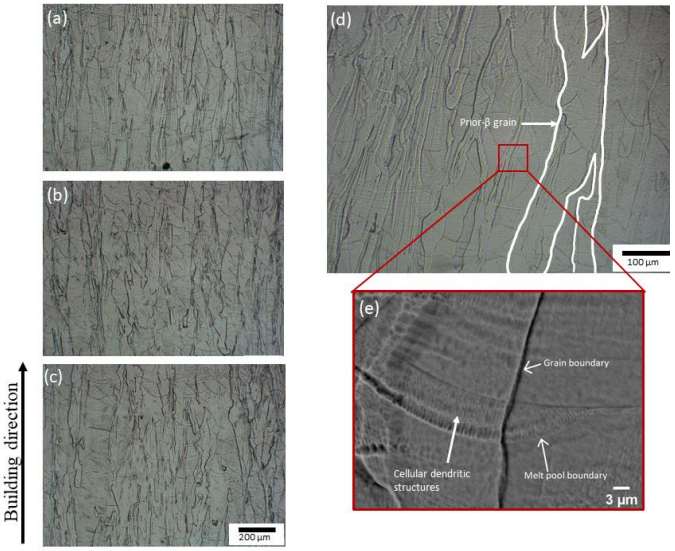

Fig. 3. Cross-section metallographs showing the microstructure of the cube in the (a) top, (b) middle, and (c) bottom regions. Higher magnification image showing (d) the columnar prior-β grain structure and (e) grain and melt pool boundaries, and cellular dendritic structures are seen along the melt pool boundaries within the grain

3.3. Microhardness measurements

Microhardness measurements along the build direction are seen in Fig. 4. Local variation in the measurements is common in L-PBF due to the complex thermal histories of the specimen. The values were comparable to the highest values reported in the literature and ranged between 260-300 HV, with low variation seen along the build direction [8], [12].

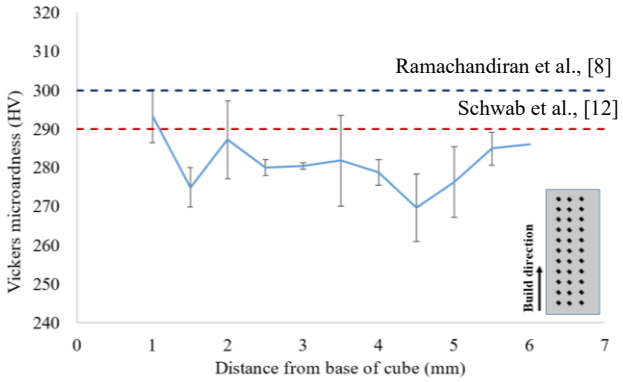

Fig. 4. Vickers microhardness along the build direction

3.4. Tensile properties

The engineering stress-strain plot of as-fabricated samples oriented parallel (0°) and perpendicular (90°) to the build direction is seen in Fig. 5 at both room temperature (RT) and sub-zero temperature (SZT) conditions.

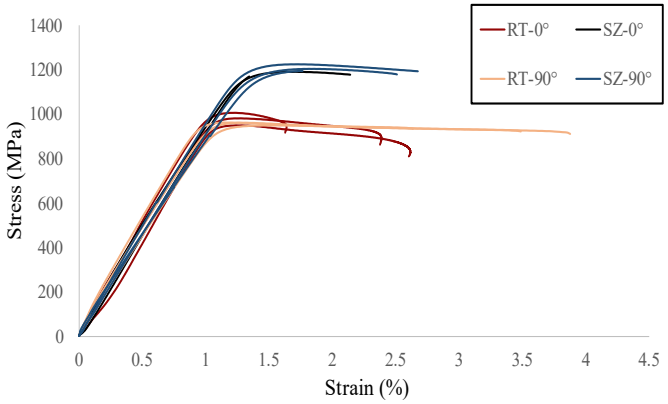

Fig. 5. Engineering stress-strain curves of tensile samples at 0°, 90°, and different testing conditions (RT: room temperature, SZT: sub-zero temperature)

At both RT and SZT, a small difference in yield and elongation between the two orientations was observed, with higher strength values in the 0° samples compared to 90°; the opposite was obtained for elongation. An average yield strength of 975.7 ± 30.1 MPa, and elongation at breakage of 2.2 ± 0.5 % for 0° samples were measured. In contrast, yield strength of 951.7 ± 12.9 MPa, and elongation at breakage of 3.4 ± 0.6 % for 90° samples were measured. At SZT, both orientations exhibit a comparable trend.

The yield strength obtained in the current work was higher than the values reported in the literature and comparable with traditional forging. To compare, the yield strengths for L-PBF are reported to be between 800 MPa and 850 MPa, with an elongation at breakage of 14-20 %. In contrast, according to the literature, the alloy processed with traditional forging exhibits general properties in the range of 1000-1100 MPa and 6-8%, respectively [9], [17], [18].

At SZT, significant yield strength increases are observed along with a decrease in ductility. The material exhibits a yield strength of 1170.5 ± 2.1 MPa and elongation of 1.7 ± 0.5 % when tested at 0°, and 1201.5 ± 26.2 MPa, 2.3 ± 0.5 % when tested at 90°. The present study's strength and elongation at breakage findings are listed in Table 4 and compared with those observed in previous literature.

Fractography of fractured surfaces at RT (Fig. 6 a, b, e, & f) shows mostly shallow cleavages with small areas of dimples, indicating a mixed failure mode dominated by brittle fractures. On the other hand, SZT (Fig. 6 c, d, g, &h) exhibits similar cleavages accompanied by small areas of dimples. However, they are also accompanied by needle-like brittle structures seen throughout the surface.

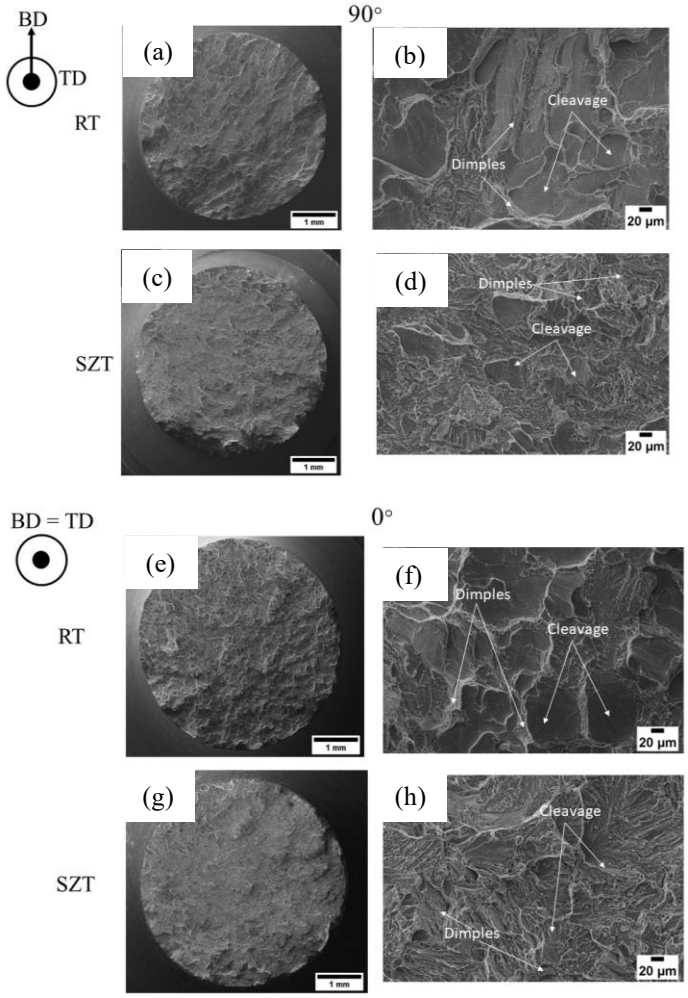

Fig. 6. Fractography of tensile samples of (a), (b) RT- 0°; (c), (d) SZT-0°; (e) (f) RT-90°; and (g), (h) SZT-90° (RT: room temperature, SZT: sub-zero temperature; 0°: tensile sample parallel to build directional, 90°: specimen perpendicular to building direction)

Table 4. Tensile properties at different orientations and testing conditions obtained in present work and comparison with the literature of L-PBF Ti-5553 alloy.

Condition	Mode	Heat treatment	UTS (MPa)	YS (MPa)	El (%)	Ref.
RT- 0°	PW	As-built	978.3 ± 28.1	975.7 ± 30.1	2.2 ± 0.5	present
RT- 90°	PW	As-built	957.3 ± 7.2	951.7 ± 12.9	3.4 ± 0.6	present
SZT- 0°	PW	As-built	1172.3 ± 16.3	1170.5 ± 2.1	1.7 ± 0.5	present
SZT- 90°	PW	As-built	1207.0 ± 15.4	1201.5 ± 26.2	2.3 ± 0.5	present
RT- 0°	PW	As-built	846	820	17	[9]
RT- 90°	PW	As-built	855	840	20	[9]
RT- 0°	CW	Preheating at 500°C	800	NA	14	[17]
RT- 90°	PW	ST at 1000°C	780	780	24	[9]
RT-0°	CW	ST at 800°C and aged at 500°C; machined	NA	1410± 8	2 ± 0.5	[19]
RT-0°	CW	HT at 400 °C	1190 ± 80	1178	1.9 ± 0.1	[20]
Forged	NA	Annealed	1175-1300	1000-1100	6-8	[18]

(ST: Solution treated, HT: Heat treated)

At room temperature, phase distribution within the titanium alloy significantly impacts the resulting mechanical [18], [20]. Even in β-alloys like Ti-5553, alpha particles at grain boundaries and within the matrix result in high strength with low ductility. Furthermore, metastable β Ti alloys are temperature sensitive, the β phase found at room temperature readily decomposes on exposure to elevated temperatures [21]. As seen in Table 4, the as-built RT results achieved in this work were comparable to the post-processed heat-treated samples at a relatively low temperature of 400-600 °C [19], [20], [22]. Heat-treatable materials are known to have distinctive mechanical properties based on the laser emission mode and preheating conditions employed [23], [24]. The process employed in the current work, in lieu of any preheating, results in properties similar to heat treatments at low temperatures. And the effect of any subsequent post-processing heat treatment would be different and should be studied.

Similarly, the stability of the β phase in metastable Ti alloys is sensitive to low temperatures. Martensitic transformation is observed as the temperature decreases in other similar alloys, with the increase in strength at the expense of ductility widely observed at sub-zero temperatures. Depending on the initial phases, temperature, and stresses applied, β phase can transform into ω phase precipitates, which significantly increase tensile strength while maintaining the ductility, or into martensitic α precipitates, resulting in a sharp loss of ductility with an increase in strengths [25], [26].

4. Conclusion

The present work aimed to study the mechanical properties of L-PBF Ti-5553 alloy at sub-zero temperatures. Fully dense samples were produced using the pulsed wave emission. Microstructure, grain morphology, and microhardness were characterized. Tensile properties at room temperature and sub-zero conditions were evaluated.

The following conclusion can be drawn:

- Highly dense (> 99.7 %) cubes were fabricated in the current work, with the interaction between exposure time and pulse duration having a significant effect on the density levels.
- Microstructure showed irregular columnar grains oriented along the build direction and growing through several layers. Cellular structures were seen at the melt pool boundary.
- Microhardness values were found between 250-300 HV with low variation along the build direction.
- Uniaxial tensile test at room temperature showed high strength, with yield strength of 975.7 ± 30.1 MPa in orientation along the build direction, while 951.7 ± 12.9 MPa perpendicular to the build direction was observed.
- Significant impact of low-temperature conditions was observed for tensile properties of Ti-5553. At sub-zero temperatures of -50°C, an increase in the tensile strength of ~26 % was seen in both the 0° and 90° samples, with ~30 % reduction in ductility.
- Fracture surfaces showed mixed failure dominated by a brittle fracture with small sections of ductile fracture.

Future works will investigate possible post-processing heat treatments and their effect on mechanical properties. Moreover, a further detailed investigation is needed to understand the phase distribution within the specimen before and after tensile testing and at RT and SZT conditions to better understand the tensile phenomenon.

Acknowledgments

This work was supported by European Space Agency under the project "Development of new metallic alloys for additive manufacturing".

References

[1] J. C. Sabol, T. Pasang, W. Z. Misiolek, and J. C. Williams, "Localized tensile strain distribution and metallurgy of electron beam welded Ti-5Al-5V-5Mo-3Cr titanium alloys," *J Mater Process Technol*, vol. 212, no. 11, pp. 2380–2385, Nov. 2012, doi: 10.1016/J.JMATPROTEC.2012.06.023.

[2] R. R. Boyer, "An overview on the use of titanium in the aerospace industry," *Materials Science and Engineering: A*, vol. 213, no. 1–2, pp. 103–114, Aug. 1996, doi: 10.1016/0921-5093(96)10233-1.

[3] R. R. Boyer, "Aerospace applications of beta titanium alloys," *JOM*, vol. 46, no. 7, pp. 20–23, Jul. 1994, doi: 10.1007/BF03220743/METRICS.

[4] J. D. Cotton *et al.*, "State of the Art in Beta Titanium Alloys for Airframe Applications," *JOM*, vol. 67, no. 6. Minerals, Metals and Materials Society, pp. 1281–1303, Jun. 11, 2015. doi: 10.1007/s11837-015-1442-4.

[5] M. B. Bettaieb, A. Lenain, and A. M. Habraken, "Static and fatigue characterization of the Ti5553 titanium alloy," *Fatigue Fract Eng Mater Struct*, vol. 36, no. 5, pp. 401–415, May 2013, doi: 10.1111/ffe.12011.

[6] E. Tunca, H. Kafali, G. Keskin, and M. C. Kuşhan, "Landing Gear Systems in Aircraft," 2022, pp. 153–179. doi: 10.1007/978-3-030-91873-6_7.

[7] J. C. Fanning, "Properties of TIMETAL 555 (Ti-5Al-5Mo-5V-3Cr-0.6Fe)," in *Journal of Materials Engineering and Performance*, Dec. 2005, pp. 788–791. doi: 10.1361/105994905X75628.

[8] N. Ramachandiran, H. Asgari, F. Dibia, R. Eybel, A. Gerlich, and E. Toyserkani, "Effect of non-lamellar α precipitate morphology on the mechanical properties of Ti5553 parts made by laser powder-bed fusion at high laser scan speeds," *Materials Science and Engineering A*, vol. 841, Apr. 2022, doi: 10.1016/j.msea.2022.143039.

[9] A. Zafari, E. W. C. Lui, M. Li, and K. Xia, "Enhancing work hardening and ductility in additively manufactured β Ti: roles played by grain orientation, morphology and substructure," *J Mater Sci Technol*, vol. 105, pp. 131–141, Apr. 2022, doi: 10.1016/j.jmst.2021.08.006.

[10] S. Bakhshivash *et al.*, "Printability and microstructural evolution of Ti-5553 alloy fabricated by modulated laser powder bed fusion," *International Journal of Advanced Manufacturing Technology*, vol. 103, no. 9–12, pp. 4399–4409, Aug. 2019, doi: 10.1007/s00170-019-03847-3.

[11] C. Zopp, S. Blümer, F. Schubert, and L. Kroll, "Processing of a metastable titanium alloy (Ti-5553) by selective laser melting," *Ain Shams Engineering Journal*, vol. 8, no. 3, pp. 475–479, 2017, doi: 10.1016/j.asej.2016.11.004.

[12] H. Schwab, M. Bönisch, L. Giebeler, T. Gustmann, J. Eckert, and U. Kühn, "Processing of Ti-5553 with improved mechanical properties via an in-situ heat treatment combining selective laser melting and substrate plate heating," *Mater Des*, vol. 130, no. May, pp. 83–89, 2017, doi: 10.1016/j.matdes.2017.05.010.

[13] L. Caprio, A. G. Demir, and B. Previtali, "Influence of pulsed and continuous wave emission on melting efficiency in selective laser melting," *J Mater Process Technol*, vol. 266, pp. 429–441, Apr. 2019, doi: 10.1016/J.JMATPROTEC.2018.11.019.

[14] L. P. Rink and L. G. Vertyukova, "Titanium alloys for cryogenic technology," *Metal Science and Heat Treatment*, vol. 9, no. 6, pp. 443–445, Jun. 1967, doi: 10.1007/BF00657591/METRICS.

[15] G. Perry, "Wheel-well and cargo compartment temperatures of large aircraft in flight: Implications for stowaways," *Aviat Space Environ Med*, vol. 73, no. 7, pp. 673–676, 2002.

[16] A. Zafari *et al.*, "Hybridisation of microstructures from three classes of titanium alloys," *Materials Science and Engineering: A*, vol. 788, p. 139572, Jun. 2020, doi: 10.1016/J.MSEA.2020.139572.

[17] H. Schwab, F. Palm, U. Kühn, and J. Eckert, "Microstructure and mechanical properties of the near-beta titanium alloy Ti-5553 processed by selective laser melting," *Mater Des*, vol. 105, pp. 75–80, 2016, doi: 10.1016/j.matdes.2016.04.103.

[18] J. C. Colombo-Pulgarín *et al.*, "Beta Titanium Alloys Processed By Laser Powder Bed Fusion: A Review," *Journal of Materials Engineering and Performance*, vol. 30, no. 9. Springer, pp. 6365–6388, Sep. 01, 2021. doi: 10.1007/s11665-021-05800-6.

[19] N. Ramachandiran *et al.*, "Influence of α case and transition zone microstructures on tensile properties in laser powder bed fused and heat-treated Ti-5553 parts," *Mater Charact*, vol. 199, p. 112834, May 2023, doi: 10.1016/j.matchar.2023.112834.

[20] H. D. Carlton, K. D. Klein, and J. W. Elmer, "Evolution of microstructure and mechanical properties of selective laser melted Ti-5Al-5V-5Mo-3Cr after heat treatments," *https://doi.org/10.1080/13621718.2019.1594589*, vol. 24, no. 5, pp. 465–473, Jul. 2019, doi: 10.1080/13621718.2019.1594589.

[21] R. R. Boyer and J. Foltz, "Effect of Heat Treatment on Mechanical Properties of Titanium Alloys," *Heat Treating of Nonferrous Alloys*, pp. 555–572, Dec. 2016, doi: 10.31399/ASM.HB.V04E.A0006270.

[22] N. Ramachandiran *et al.*, "Effects of post heat treatment on microstructure and mechanical properties of Ti5553 parts made by laser powder bed fusion," *J Alloys Compd*, vol. 938, p. 168616, Mar. 2023, doi: 10.1016/J.JALLCOM.2022.168616.

[23] F. Belloli, A. G. Demir, and B. Previtali, "Understanding the deformation mechanisms of horizontal internal channels during the LPBF of 18Ni300 maraging steel," *J Manuf Process*, vol. 71, pp. 237–248, Nov. 2021, doi: 10.1016/J.JMAPRO.2021.07.063.

[24] A. G. Demir and B. Previtali, "Investigation of remelting and preheating in SLM of 18Ni300 maraging steel as corrective and preventive measures for porosity reduction," *International Journal of Advanced Manufacturing Technology*, vol. 93, no. 5–8, pp. 2697–2709, Nov. 2017, doi: 10.1007/S00170-017-0697-Z/METRICS.

[25] Y. Li, Z. Liao, W. Zhang, Z. Wu, and C. Zhou, "Strength-ductility synergy in a metastable β titanium alloy by stress induced interfacial twin boundary ω phase at cryogenic temperatures," *Materials*, vol. 13, no. 21, pp. 1–8, Nov. 2020, doi: 10.3390/ma13214732.

[26] W. dong Zhang, Z. Wu, Y. Liu, H. Bei, B. Liu, and J. Qiu, "Plastic deformation mechanism of Ti–Nb–Ta–Zr–O alloy at cryogenic temperatures," *Materials Science and Engineering: A*, vol. 765, p. 138293, Sep. 2019, doi: 10.1016/J.MSEA.2019.138293.